Characterization of Levitated Superfluid Helium Drops in High Vacuum

C. D. Brown,[1,2,3] Y. Wang,[4] M. Namazi,[4,6] G. I. Harris,[4,5] M. T. Uysal,[4] and J. G. E. Harris[1,4,6]
[1]*Department of Physics, Yale University, New Haven, CT 06520*
[2]*Department of Physics, University of California, Berkeley CA 94720*
[3]*Challenge Institute for Quantum Computation, University of California, Berkeley CA 94720*
[4]*Department of Applied Physics, Yale University, New Haven, CT 06520*
[5]*ARC Centre of Excellence for Engineered Quantum Systems, School of Mathematics and Physics, The University of Queensland, Brisbane, QLD, Australia and*
[6]*Yale Quantum Institute, Yale University, New Haven, CT 06520*
(Dated: December 18, 2021)

We describe measurements of the thermal, mechanical, and optical properties of drops of superfluid ^{4}He that are magnetically levitated in high vacuum. The drops have radius $\sim$ 200 µm, cool by evaporation to temperatures $\sim$ 330 mK, and can be trapped indefinitely in a background vapor pressure $\sim 10^{-8}$ mBar. Measurements of the drops' evaporation rate, normal modes of motion, and optical whispering gallery modes are found to agree with well-established models.

Superfluid helium drops offer a combination of isolation, low temperature, superfluidity, and experimental access that is unique among condensed matter systems. These features make it possible to address a number of questions in chemistry and physics [1, 2]. For example, such drops have been used to cool a range of molecular species to $\sim$ 400 mK, facilitating precision spectroscopy and studies of cold chemical reactions [3–6]. In addition, the drops themselves are interesting for studies of classical and quantum fluid dynamics [7–11], and may be well-suited for exploring macroscopic quantum phenomena [12].

In practice, the scientific questions that can be addressed by an isolated helium drop depend on its size, temperature, and lifetime, and on the experimental probes that can be applied to it. For example, a drop must exceed a certain size to become superfluid, or to serve as a host for chemical dopants. The drop's size also sets the frequency and energy scales of its internal excitations (such as its vorticity and the acoustic modes of its bulk and surface), and determines its ability to host optical whispering gallery modes (WGMs). Low temperature is required for the drop to become superfluid, and to isolate quantum coherent effects in the drop's excitations. Lastly, some experimental probes require the drop to be trapped; in these cases, its lifetime will be limited by its evaporation rate, which depends strongly on its temperature.

A number of methods have been used to trap superfluid drops. Electric trapping has confined mm-scale drops, but requires the drops to be charged [13]. Neutral drops may be optically trapped, but to date practical laser-power considerations have limited this approach to µm-scale drops [14]. Magnetic trapping has been used to confine cm-scale, electrically-neutral drops [15]. In principle, each of these approaches is compatible with operation in high vacuum; however, studies to date of trapped superfluid drops have been carried out in the presence of He vapor whose density is high enough that the drop is in thermal equilibrium with its enclosure.

An important alternative to trapping drops is to study them in free fall [16–22]. Freely falling droplets can be produced with radii ranging from nm to µm, typically via expansion through a nozzle into a high vacuum chamber. These droplets fall for $\sim$ 10 ms before they are destroyed, either by measurement or by colliding with the end of the chamber. In this time, the droplet's temperature $T_{\rm drop}$ is found to be accurately described by a model of free evaporation into perfect vacuum [23], with ^{4}He droplets reaching $T_{\rm drop} \sim 380$ mK.

In this paper we describe studies of mm-scale, electrically-neutral, superfluid ^{4}He drops that are trapped by diamagnetic levitation in high vacuum. We have measured their thermal, mechanical, and optical properties, including their evaporation rate, heat load, and temperature; their capillary modes and center-of-mass motion; and their medium-finesse optical WGMs. These measurements show good agreement with theoretical predictions, and demonstrate that superfluid drops can be trapped indefinitely with $T_{\rm drop} \sim 330$ mK.

A schematic illustration of the experiment is shown in Ref. [24]. Levitation is provided by a non-uniform superconducting solenoid housed in the ^{4}He bath space of a cryostat. The solenoid is designed so that stable levitation is achieved for 115 A $< I <$ 118 A, where I is the current in the solenoid. Varying I within this range translates the levitation point vertically, and can be used to vary the drop shape (i.e., from prolate to oblate) [25]. Drops are produced and trapped in a custom-built cell that fits in the cryostat's vacuum space and extends into the magnet's bore. The temperature of the cell walls $T_{\rm cell}$ is controlled by a liquid ^{4}He flow line. Optical access to the trapping region is provided by windows in the cryostat and cell [24].

To produce a levitated drop, I is fixed and the cell is cooled by the ^{4}He flow line. The cell is then filled with a controlled quantity of ^{4}He, which produces a puddle at the bottom of the cell. Next, the cell is opened to a

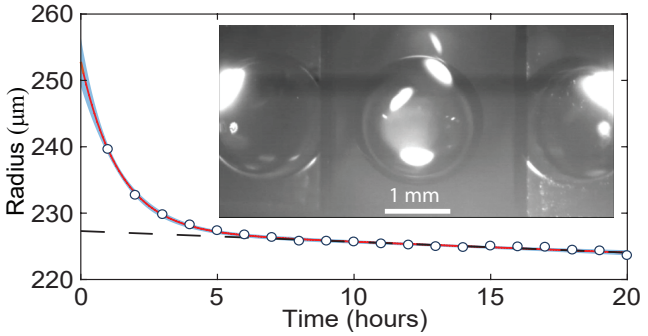

FIG. 1. A levitated drop. Inset: a ^{4}He drop shortly after it has been levitated. The central portion of the image is a direct view of the drop, while the left and right portions are the reflections from two 45° mirrors placed near the levitation region. Main figure: The drop radius R (circles) as a function of time. The red curve is a fit to the sum of an exponential and a linear function (the linear portion is the dashed line). The statistical uncertainty in R is $\sim$ 10 nm. The blue band shows the systematic uncertainty.

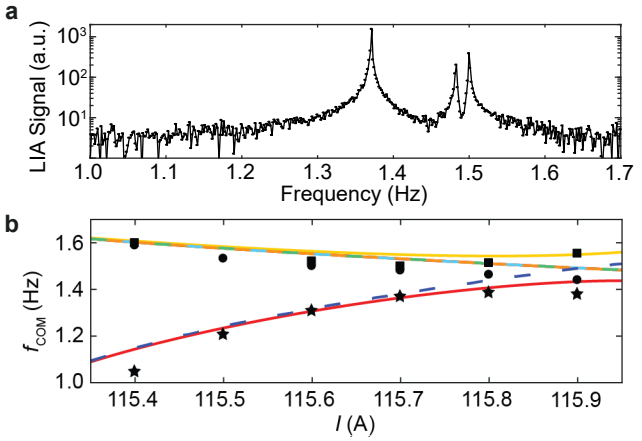

FIG. 2. Center-of-mass (COM) motion of a levitated drop. (a) The power spectral density of the COM motion for I = 115.7 A. (b) The frequencies of the normal modes versus the magnet current. Black markers: frequencies determined by fitting the data in (a). Dashed lines: the calculated radial (light blue and light green) and axial (dark blue) frequencies assuming the magnets axis is parallel to gravity. Solid lines (red, orange, yellow): the best fit of the data for a magnetic trap that is tilted with respect to gravity.

turbomolecular pump (TMP), which causes the puddle to boil aggressively. In the subsequent seconds, a fog of μm-scale droplets aggregates in the levitation region and then coalesces into a single mm-scale drop at the levitation point. The inset of Fig. 1 shows a levitated drop with $R = 1.0$ mm roughly 1 s after opening the cell to the TMP.

After the drop has been trapped, the TMP continues to evacuate the cell. After roughly five minutes the puddle is completely depleted, and $P_{\rm cell}$ decreases sufficiently that thermal contact between the drop and the cell walls is broken. The drop's thermal isolation is evidenced by the fact that R appears constant (within the resolution of the imaging system) for several hours.

However, close examination shows that the drop continues to evaporate, albeit very slowly. To measure the very slow change in R, we use standard image processing techniques [26] to determine the drop's edge in each video frame. This shape is fit to a circle, and the value of R returned by this fit is averaged over 1,200 images (acquired in 60 s) to produce each of the data points shown in Fig. 1. This data shows that the evaporation rate decreases in the first few hours after trapping, and then becomes roughly constant. A linear fit to the last 12 hours of data gives an average evaporation rate $\dot{R} = (0.44 \pm 0.04)$ Å/s. According to the model described in Ref. [23], this corresponds to $T_{\rm drop} \approx 330$ mK and a heat load $\dot{Q} \sim 30$ pW on the drop. As described below, the likely source of this heat is residual He vapor in the cell.

The drop's center-of-mass (COM) motion is measured using a diode laser (DL) with wavelength $\lambda = 1,064$ nm which passes though the drop so that it is refracted by an angle that depends on the drop's position. This deflection is measured using a photodiode [24].

Fig. 2a shows a typical spectrum of the COM motion. No deliberate drive was applied to the drop; the observed motion is the drop's steady-state response to vibrations in the cryostat. For each value of I, the data show peaks corresponding to the three normal modes of motion in the trap. The resonant frequencies $f_{\rm COM}$ of these modes are shown as a function of I in Fig. 2b. The dashed lines are the frequencies calculated (without free parameters) for a trapping field whose symmetry axis is colinear with gravity. In this model, the radial and axial frequencies are $\omega_r = (-\chi/(\mu_0\rho)(1/2(\partial_z B_z)^2 - B_z\partial_{zz}B_z))^{1/2}$ and $\omega_z = (-2\chi/(\mu_0\rho)((\partial_z B_z)^2 + B_z\partial_z B_z))^{1/2}$ respectively, where $\rho = 145$ kg/m^3 is the density of liquid ^{4}He and $\chi = -1.89 \times 10^{-6}$ is the volume diamagnetic susceptibility of ^{4}He. The magnetic field and its derivatives are evaluated at the levitation point [26] (the numerical values of these quantities are known from the magnet design).

While this model reproduces the qualitative features in the $f_{\rm COM}(I)$, it does not capture their behavior near the predicted degeneracy at $I = 115.9$ A. The solid lines in Fig. 2b show a fit to a model that incorporates a relative angle θ between gravity and the trap's symmetry axis [26]. Using θ as a fitting parameter returns $\theta = (0.27 \pm 0.11)°$. This misalignment may result from an actual tilt of the cryostat, or from deformation of the trapping fields due to the magnetic response of the cell materials.

The drops levitated here are nearly spherical, with index of refraction $n_{\rm He} = 1.028$ for visible and near-infrared wavelengths, and vanishingly small absorption (predicted to be $\sim 10^{-9}$ m^{-1} for $T_{\rm drop} = 330$ mK [14, 27]). As a

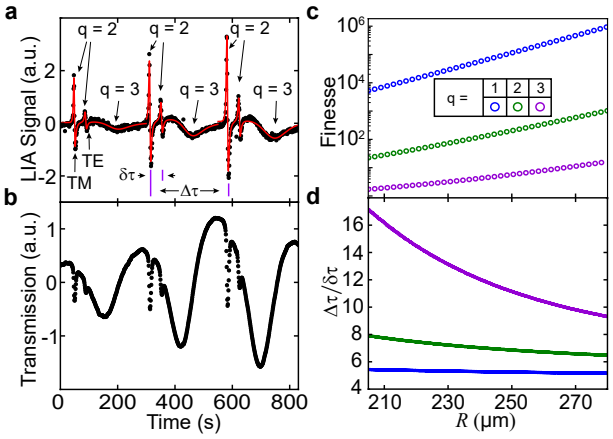

FIG. 3. Optical WGMs. (a) The lock-in signal produced by optical transmission through a superfluid drop with $R = 240 \pm 1$ μm. (b) The integral of the data in (a). (c) The calculated finesse for WGMs with $q \in \{1, 2, 3\}$. (d) The calculated splitting between TE and TM modes, $\Delta\tau/\delta t$, with $q \in \{1, 2, 3\}$.

result they are expected to host optical WGMs whose finesse increases rapidly with R for $R > 0.1$ mm [12].

To characterize these WGMs, we use the setup shown in the SI. The DL is focused at the center of the drop and its intensity is modulated at a frequency close to the resonance of the drop's $\ell_{\rm cap} = 2$ capillary mode (described below). The optical dipole force exerted by the DL beam excites this capillary mode, which effectively modulates R (more precisely, the drop's circumference in the plane of the WGM is modulated). At the same time, an intensity-stabilized HeNe laser ($\lambda = 633$ nm) is focused at the drop's edge, and its transmission is recorded using a lock-in amplifier (LIA). In addition to the modulation produced by the drop's capillary mode, the drop's evaporation causes R to slowly decrease with time. As a result, the LIA signal is approximately proportional to the derivative of the drop's transmission with respect to R.

Fig. 3a shows a typical record from the LIA for a drop trapped with $I = 116$ A. Analysis of video images taken during these measurements gives $R = 240 \pm 1$ μm. Fig. 3b shows the same data integrated with respect to time, giving a signal proportional to the optical transmission through the drop. The data show a pattern of features that repeats with a period $\Delta\tau \sim 300$ s. Each feature corresponds to a WGM being tuned through resonance with the HeNe by the drop's evaporation. Each repetition of the pattern corresponds to the drop's circumference changing by $\lambda_{\rm HeNe}/n_{\rm He}$ (equivalent to the WGM's angular index $\ell \approx 2,380$ changing by 1), which tunes the cavity through one free spectral range (FSR).

Within each of the three FSRs shown in Fig. 3a, the data is fit to the sum of three (once-differentiated) Lorentzians, with each Lorentzian's center position, linewidth, and amplitude used as fit parameters. The result is the red curve in Fig. 3a. These fits give the finesse $\mathcal{F} = 36 \pm 2$ for the largest feature, $\mathcal{F} = 30 \pm 3$ for the middle feature, and $\mathcal{F} = 1.9 \pm 0.1$ for the broadest feature. These value are the averages over the three FSRs shown in Fig. 3a.

To determine the identities of these modes, Fig. 3c shows the calculated $\mathcal{F}$ for WGMs in a sphere with index of refraction 1.028, as a function of the sphere's radius [28]. Results are shown for both TE and TM polarizations, and for values of the WGM's radial index $q \in \{1, 2, 3\}$ (where $q - 1$ gives the number of a radial electric field nodes within the drop). Fig. 3d shows the calculated splitting between TE and TM modes (having all other mode indices equal). These plots indicate that the broadest feature in each FSR corresponds to $q = 3$ modes (their linewidth is too large to resolve the TE and TM modes separately), and that the two narrower features correspond to TE and TM modes with $q = 2$.

The measured linewidths of these $q = 2$ modes are roughly three times greater than in the calculation shown in Fig. 3c. This is consistent with the small ellipticity ($\epsilon \sim 10^{-5}$) expected for this value of R and I [25]. Specifically, ϵ splits the degeneracy over the WGM's azimuthal index m into resonances whose splittings (i.e. between modes with m differing by ± 1) are all much smaller than the expected WGM linewidth. As a result, they form an unresolved band whose width would correspond to an apparent finesse $\mathcal{F}_\epsilon = 46$ for the $q = 2$ modes.

The fit in Fig. 3a also gives the ratio between the FSR and the splitting between the TE and TM $q = 2$ modes as 6.6 ± 0.1. This is in good agreement with the calculated value of 6.9 (Fig. 3d).

We did not observe the $q = 1$ WGMs, whose finesse is expected to be $\sim 10^4$. This is likely because of poor mode-matching between these modes and the HeNe beam, and because the drop's evaporation tuned these modes through resonance too quickly to be recorded with our data sampling rate (1 Hz).

Since the passage of each FSR corresponds to the drop circumference changing by $\lambda_{\rm HeNe}/n_{\rm He}$, we can use $\Delta\tau$ as a measurement of the drop's evaporation rate $\dot{R} = \lambda_{\rm HeNe}/2\pi n_{\rm He}\Delta\tau$. The evaporation model given in Refs. [12, 23] can then be used to infer $T_{\rm drop}$ and $\dot{Q}$ from $\dot{R}$.

This approach is illustrated in Fig. 4, which shows data for a drop with $R = 207.5 \pm 1$ μm (as determined by image analysis). The optical transmission through this drop (not shown) has features similar to those in Fig. 3a, which are fit to determine $\Delta\tau$. Figs. 4a,b show $T_{\rm drop}$ and $\dot{Q}$ inferred in this manner as a function of $P_{\rm DL}$, the power of the DL incident on the drop. The data are consistent with a heat load proportional to $P_{\rm DL}$, along with a background heat load ~ 35 pW. While the former contribution could reflect absorptive heating of the drop

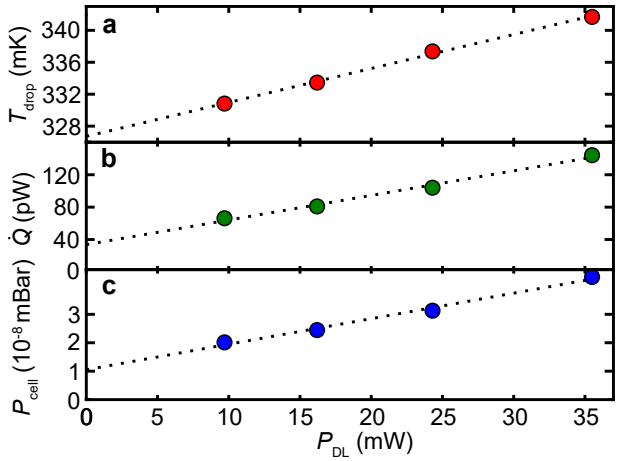

FIG. 4. The drop's thermal properties. (a) The drop temperature. (b) The heat load on the drop. (c) The background pressure in the cell. These quantities are obtained from measurements of $\dot{R}$, and are plotted as a function of the power of the laser incident on the drop. The dashed lines are linear fits.

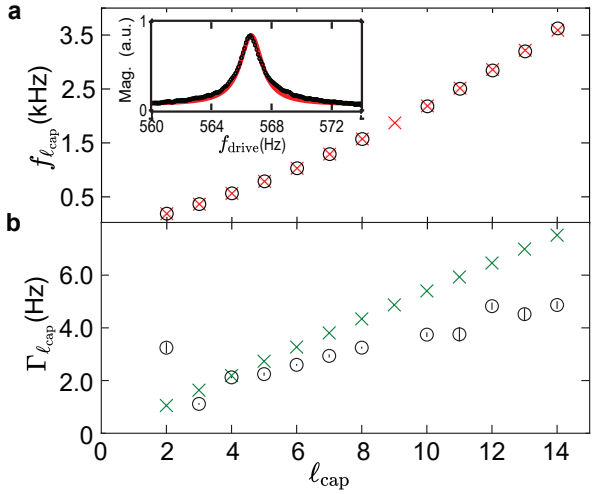

FIG. 5. Capillary mode resonances. (a) The measured (circles) and expected (crosses) resonance frequencies. Inset: the resonance of the $\ell_{vib} = 4$ mode (black), along with the best fit (red). (b) The measured (circles) and expected (crosses) damping rates.

by the DL, the coefficient of proportionality (3×10^{-9}) is roughly three orders of magnitude greater than expected [14, 27]. If, instead, the observed heatload is attributed to He gas in the cell (assumed to be at the temperature of the cell walls), the corresponding pressure P_{cell} is shown in Fig. 4c. We attribute the increase in P_{cell} with increasing P_{DL} to the absorption of laser light by various objects in the cell.

Vibrations of the drop for which the restoring force is dominated by surface tension are known as capillary modes. These modes' oscillation frequencies are given by

$$f_{\ell_{cap}} = \sqrt{\ell_{cap}(\ell_{cap}+1)(\ell_{cap}-2)\sigma/4\pi^2\rho R^3} \qquad (1)$$

where $\ell_{cap} \in \{2, 3, 4, ...\}$ and $\sigma = 3.75 \times 10^{-4}$ J/m^2 is the surface tension of superfluid liquid ^{4}He [29]. To drive these modes, the DL is focused at the drop's center and its intensity is modulated at frequency f_{drive}. The modes' response is monitored by recording the transmission of the HeNe beam through the drop. This beam's position is chosen to avoid the optical WGMs, so its transmission is modulated because the capillary modes deflect the beam.

Fig. 5 shows the frequencies and linewidths of the first several resonances measured in a drop with $R = 246 \pm 0.7$ μm and $T_{drop} \approx 330$ mK. The frequencies and linewidths are determined by fitting each resonance. Assuming that each resonance corresponds to a distinct value of ℓ_{cap} (except for $\ell_{cap} = 9$, which did not produce a measurable signal) the resonance frequencies are found to agree with Eq. 1 to better than 1%.

These modes' linewidths $\Gamma_{\ell_{cap}}$ are shown in Fig. 5b, along with the values expected from the damping of capillary modes by inelastic scattering of thermal phonons from the drop's surface: [30]

$$\frac{\Gamma_{\ell_{cap}}}{2\pi} = \frac{\pi^2\hbar\mathcal{K}}{60\rho_0}\left(\frac{k_B T}{\hbar u_c}\right)^4, \qquad (2)$$

where $\mathcal{K} = (\ell_{cap}(\ell_{cap}-1)(\ell_{cap}+2))^{1/3}/R$ and $u_c = 238$ m/s is the speed of sound in liquid ^{4}He. While this prediction shows qualitative agreement with the data, we note two discrepancies. The first is in the average slope of $\Gamma_{\ell_{cap}}$ vs. ℓ_{cap}. This slope is predicted to be $\propto T_{drop}^{-4}$, and would agree with the observed slope if one were to take $T_{drop} = 310$ mK. However this would correspond to an evaporation rate $\sim 4\times$ smaller than observed. The second discrepancy is in the damping rates for $\ell_{cap} = 2$ and $\ell_{cap} = 3$, which depart from the simple trend predicted by Eq. 2.

Both discrepancies may have their origin in the fact that Eq. 2 is derived under the assumption that phonons which are inelastically scattered by the surface fully thermalize before being scattered again. However the mean free path of phonons $\Lambda \propto T^{-4}$, with $\Lambda = 4.5$ mm for $T = 330$ mK [31]. Furthermore the phonon thermalization time $\Lambda/u_c \approx 16$ μs $\ll f_{\ell_{cap}}^{-1}$ for $2 \le \ell_{cap} \le 14$. Thus, a thermal phonon in the drops studied here will scatter many times from an effectively stationary drop surface. The damping of capillary modes in this regime has not been calculated.

In conclusion, these results show that drops of superfluid ^{4}He can be magnetically levitated in high vacuum with indefinitely long lifetime, and that their thermal, optical, and mechanical properties are consistent with expectations. We expect that modest improvements in the design of the experimental cell will reduce the density of background He gas, resulting in lower drop temperature

and correspondingly lower rates of mechanical damping and evaporation. In addition, the use of *in situ* mode-matching optics and improved data acquisition should allow access to the drops' high-finesse $q = 1$ WGMs. The realization of such WGMs in objects whose stiffness is set only by the weak surface tension of liquid helium may provide access to new regimes of cavity optomechanics.

We acknowledge helpful discussions with Florian Marquardt, Andrea Aiello, Lilian Childress, Aaron Hillman, Yogesh Patil, Vincent Bernardo, David Johnson, Craig Miller, Rosario Bernardo, and Leonid Glazman. We acknowledge support from W. M. Keck Foundation Grant No. DT121914, AFOSR Grant No. FA9550-15-1-0270, DARPA Grant No. W911NF-14-1-0354, ARO Grant No. W911NF-13-1-0104, NSF Grant No. 1707703, ONR Grant N00014-18-1-2409, and Vannevar Bush Faculty Fellowship N00014-20-1-2628. This project was made possible through the support of a grant from the John Templeton Foundation. This material is based upon work supported by the NSF Graduate Research Fellowship under Grant No. DGE-1122492 and by a Ford Foundation Dissertation Fellowship.

[1] R. M. P. Tanyag, C. F. Jones, C. Bernando, S. M. O'Connell, D. Verma, and A. F. Vilesov, Cold chemistry: molecular scattering and reactivity near absolute zero **11**, 389 (2017).

[2] J. A. Northby, Journal of Chemical Physics **115**, 10065 (2001).

[3] F. Stienkemeier and K. K. Lehmann, Journal of Physics B-Atomic Molecular and Optical Physics **39**, R127 (2006).

[4] C. Callegari, K. K. Lehmann, R. Schmied, and G. Scoles, Journal of Chemical Physics **115**, 10090 (2001).

[5] E. Lugovoj, J. P. Toennies, and A. Vilesov, Journal of Chemical Physics **112**, 8217 (2000).

[6] J. P. Toennies and A. F. Vilesov, Annual Review of Physical Chemistry **49**, 1 (1998).

[7] S. M. O. O'Connell, R. M. P. Tanyag, D. Verma, C. Bernando, W. Pang, C. Bacellar, C. A. Saladrigas, J. Mahl, B. W. Toulson, Y. Kumagai, P. Walter, F. Ancilotto, M. Barranco, M. Pi, C. Bostedt, O. Gessner, and A. F. Vilesov, Phys. Rev. Lett. **124**, 215301 (2020).

[8] L. F. Gomez, K. R. Ferguson, J. P. Cryan, C. Bacellar, R. M. P. Tanyag, C. Jones, S. Schorb, D. Anielski, A. Belkacem, C. Bernando, R. Boll, J. Bozek, S. Carron, G. Chen, T. Delmas, L. Englert, S. W. Epp, B. Erk, L. Foucar, R. Hartmann, A. Hexemer, M. Huth, J. Kwok, S. R. Leone, J. H. S. Ma, F. R. N. C. Maia, E. Malmerberg, S. Marchesini, D. M. Neumark, B. Poon, J. Prell, D. Rolles, B. Rudek, A. Rudenko, M. Seifrid, K. R. Siefermann, F. P. Sturm, M. Swiggers, J. Ullrich, F. Weise, P. Zwart, C. Bostedt, O. Gessner, and A. F. Vilesov, Science **345**, 906 (2014).

[9] S. Chandrasekhar, Proceedings of the Royal Society of London. Series A. Mathematical and Physical Sciences **286**, 1 (1965).

[10] R. A. Brown and L. E. Scriven, Proceedings of the Royal Society of London Series a-Mathematical Physical and Engineering Sciences **371**, 331 (1980).

[11] C. J. Heine, Ima Journal of Numerical Analysis **26**, 723 (2006).

[12] L. Childress, M. P. Schmidt, A. D. Kashkanova, C. D. Brown, G. I. Harris, A. Aiello, F. Marquardt, and J. G. E. Harris, Physical Review A **96** (2017), ARTN 063842 10.1103/PhysRevA.96.063842.

[13] J. J. Niemela, Journal of Low Temperature Physics **109**, 709 (1997).

[14] M. A. Weilert, D. L. Whitaker, H. J. Maris, and G. M. Seidel, Journal of Low Temperature Physics **98**, 17 (1995).

[15] M. A. Weilert, D. L. Whitaker, H. J. Maris, and G. M. Seidel, Physical Review Letters **77**, 4840 (1996).

[16] H. Buchenau, E. L. Knuth, J. Northby, J. P. Toennies, and C. Winkler, Journal of Chemical Physics **92**, 6875 (1990).

[17] W. Schollkopf and J. P. Toennies, Science **266**, 1345 (1994).

[18] J. Braun, P. K. Day, J. P. Toennies, G. Witte, and E. Neher, Review of Scientific Instruments **68**, 3001 (1997).

[19] J. P. Toennies, A. F. Vilesov, and K. B. Whaley, Physics Today **54**, 31 (2001).

[20] J. P. Toennies and A. F. Vilesov, Angewandte Chemie-International Edition **43**, 2622 (2004).

[21] A. Kautsch, M. Koch, and W. E. Ernst, Physical Chemistry Chemical Physics **17**, 12310 (2015).

[22] P. Thaler, A. Volk, D. Knez, F. Lackner, G. Haberfehlner, J. Steurer, M. Schnedlitz, and W. E. Ernst, Journal of Chemical Physics **143** (2015), Artn 134201 10.1063/1.4932182.

[23] D. M. Brink and S. Stringari, Zeitschrift Fur Physik D-Atoms Molecules and Clusters **15**, 257 (1990).

[24] See supplemental material.

[25] M. A. Weilert, D. L. Whitaker, H. J. Maris, and G. M. Seidel, Journal of Low Tempearture Physics **106**, 101 (1997).

[26] C. D. Brown II, *Optical, Mechanical and Thermal Properties of Superfluid Helium Drops Magnetically Levitated in Vacuum*, Ph.D. thesis, Yale University (2019).

[27] G. Seidel, R. Lanou, and W. Yao, Nuclear Instruments and Methods in Physics Research Section A: Accelerators, Spectrometers, Detectors and Associated Equipment **489**, 189 (2002).

[28] A. N. Oraevsky, Quantum Electronics **32**, 377 (2002).

[29] C. Vicente, W. Yao, H. J. Maris, and G. M. Seidel, Phys. Rev. B **66**, 214504 (2002).

[30] P. Roche, M. Roger, and F. I. B. Williams, Physical Review B **53**, 2225 (1996).

[31] H. J. Maris, Reviews of Modern Physics **49**, 341 (1977).